LINEARIZED AVA INVERSION OF PP AND PS REFLECTIONS FROM LOW-VELOCITY TARGETS USING ZOEPPRITZ EQUATIONS

XINFA ZHU, GEORGE A. MCMECHAN and TING GONG

Center for Lithospheric Studies, The University of Texas at Dallas, 800 West Campbell Road (ROC21), Richardson, TX 75080-3021, U.S.A. xinfazhu@gmail.com

(Received March 26, 2014; revised version accepted June 5, 2014)

ABSTRACT

Zhu, X., McMechan, G.A. and Gong, T., 2014. Linearized AVA inversion of PP and PS reflections from low-velocity targets using Zoeppritz equations. *Journal of Seismic Exploration*, 23: 313-339.

The top of a reservoir is often a seismic interface of decreasing velocity. No critical angle exists in reflections from such an interface, and so Zoeppritz reflection coefficients are closed-form and accurate at all incident angles and frequencies. However, most existing AVO methods use approximations to the Zoeppritz equations. These approximations assume small contrasts and small angles, and the number of invertible parameters is usually limited to two or three (the so-called two- or three-term AVO). We propose using the Zoeppritz equations for amplitude inversion of target reflections without critical angles. The Fréchet derivatives are calculated analytically. We use a linearized iterative least-squares inversion scheme. This algorithm is applicable to PP, PS, SS, and SP reflections. We demonstrate that PP amplitude data can be inverted for four parameters (three velocity ratios and the density ratio), although joint inversion of PP and PS reflections can greatly improve the robustness. The algorithm is superior to conventional approximations in that it works for any large (decreasing) contrasts at any large angles; it is accurate and can invert for more parameters.

KEY WORDS: AVA, joint inversion, reflection coefficients.

INTRODUCTION

Amplitude variation with offset (AVO), or with angle (AVA), have been used to invert for elastic parameters and to predict rock and fluid properties. The inversion usually minimizes the difference between the observed and synthetic (predicted) AVA data by least-squares fitting. Before input to the inversion, the observed amplitude data must be properly preprocessed. Ideally, all amplitude effects other than the reflection coefficients (RCs) should be compensated; these include geometrical spreading, attenuation, dispersion, and

0963-0651/14/$5.00

transmission losses (Deng and McMechan, 2007). In conventional AVA inversion, the predicted amplitude data are calculated with various approximations to the Zoeppritz equations (Russell et al., 2011).

Classic approximations to the Zoeppritz equations include those of Bortfeld (1961), Aki and Richards (1980), and Shuey (1985). These linear approximations decouple the elastic parameters and facilitate intuitive understanding of how the parameter changes affect the reflection amplitudes Russell et al. (2011). They are also easily applied to inversion problems thanks to the simpler equations. However, the derivation of these approximations assumes weak elastic contrasts and small incident angles. Higher-order approximations (Ursin and Dahl, 1992; Wang, 1999; Ursenbach, 2002) push the accuracy to larger angles. All these approximations break down as angles increase, especially for large elastic contrasts.

Surveys with wide acquisition apertures, such as ocean-bottom nodes (Beaudoin, 2010) and dual coil shooting (Moldoveanu et al., 2012), record large incident-angle reflections from deep structures, so provide extra independent data for AVA analysis, and make density inversion promising. Considering the accuracy limits of the approximations, the Zoeppritz equations have been explored for such large-angle AVA analysis (Zhu and McMechan, 2012a; Lehocki et al., 2013). Ma et al. (2013) use the full Zoeppritz equation in Bayesian generalized linear inversion. Zhi et al. (2013) solve the nonlinear optimization problem of using the Zoeppritz equations with a trust-region reflective Newton method (Coleman and Li, 1994).

Although more accurate than the approximations, the Zoeppritz equations also have assumptions, such as plane waves, a sharp planar interface, and infinite frequency. They do not work for spherical-wave reflections near the critical angle. The Zoeppritz RCs do not include the propagation effects in overburden (e.g., spreading, attenuation, and transmission losses), and effects of the interface dip and curvature. Before using Zoeppritz equations, we need to make sure that the model satisfies these assumptions and the observed AVA data have been properly processed to compensate for these effects.

This paper is a continuation and extension, of our work in Zhu and McMechan (2012a), to do target-oriented linearized Zoeppritz inversion. The main innovations include choosing the Zoeppritz equations over the approximations, parameterization of three velocity ratios and the density ratio, justification of applying plane-wave RCs to spherical non-critical reflections, linearization of the nonlinear Zoeppritz equations, and developing the analytical Fréchet derivatives. The system of linear equations is solved by least-squares. To invert for all the four ratios, additional independent data are required. We investigate two options: using PP alone within wide angle ranges, and using both PP and PS within less wide angle ranges. The first option requires

ultra-long offsets, while the second option requires longer recording times (to acquire the slower PS reflections).

This paper has two main sections: AVA modeling and AVA inversion. In the modeling section, we give the equations of Zoeppritz RCs and their approximations, and compare their model parameterizations. In the inversion section, we introduce the linear system: structure, calculation, and conditioning. Finally we present some inversion examples which demonstrate the new capability of our algorithm to inverting for four parameters.

AVA MODELING

Zoeppritz equations

Assume an elastic model of two half spaces in welded contact. The P-wave velocity, S-wave velocity, and density in the upper half space are denoted as α_1, β_1, and ρ_1; and in the lower half space, as α_2, β_2, and ρ_2. The plane-wave RCs for such a model are given by the Zoeppritz equations. The explicit forms for PP and PS reflection amplitudes are given by Červený et al. (1977) as:

$$\begin{aligned} R_{PP} = {} & [Q^2 - r_4T_0T_3 + r_4T_1T_2 - (1+Q)^2T_0T_2 \\ & + (r_4-Q)^2T_1T_3 - (r_4-Q-1)^2T_0T_1T_2T_3] \\ & /[Q^2 + r_4T_0T_3 + r_4T_1T_2 + (1+Q)^2T_0T_2 \\ & + (r_4-Q)^2T_1T_3 + (r_4-Q-1)^2T_0T_1T_2T_3] \quad , \end{aligned} \tag{1}$$

for the PP reflections, and

$$\begin{aligned} R_{PS} = {} & 2r_2^{-1}T_2[Q(1 + Q) + (r_4 - Q)(r4 - Q - 1)T_1T_3] \\ & /[Q^2 + r_4T_0T_3 + r_4T_1T_2 + (1+Q)^2T_0T_2 \\ & + (r_4-Q)^2T_1T_3 + (r_4-Q-1)^2T_0T_1T_2T_3] \quad , \end{aligned} \tag{2}$$

for the PS reflections, where

$$Q = 2\sin^2\theta(r_4r_3^2 - r_2^2) \quad , \tag{3a}$$

$$T_0 = r_0\sin\theta/\sqrt{(1 - r_0^2\sin^2\theta)} \quad , \tag{3b}$$

$$T_1 = r_1\sin\theta/\sqrt{(1 - r_1^2\sin^2\theta)} \quad , \tag{3c}$$

$$T_2 = r_2\sin\theta/\sqrt{(1 - r_2^2\sin^2\theta)} \quad , \tag{3d}$$

and

$$T_3 = r_3\sin\theta/\sqrt{(1 - r_3^2\sin^2\theta)} \quad , \tag{3e}$$

in which

$$r_0 = \alpha_1/\alpha_1,\ r_1 = \alpha_2/\alpha_1,\ r_2 = \beta_1/\alpha_1,\ r_3 = \beta_2/\alpha_1, \text{ and } r_4 = \rho_2/\rho_1 \ . \tag{4}$$

In eqs. (3) and (4), $r_0 = 1$ and $T_0 = \tan\theta$ are for internal consistency and symmetry of the formulation, which leaves only five independent variables: the incident angle (θ) and four ratios (r_1, r_2, r_3, r_4). Thus, the Zoeppritz RCs

$$R_{zprz} = f(\theta, r_1, r_2, r_3, r_4) \ . \tag{5}$$

At normal incidence ($\theta = 0°$), the elastic R_{PP} reduces to the acoustic reflection coefficient (Zhu and McMechan, 2012b), and no PS reflection is generated ($R_{PS} = 0$).

It is well-known that the (plane-wave) Zoeppritz RCs do not apply near the critical angle (Alhussain et al., 2008). Therefore, we assume $\alpha_2 < \alpha_1$, meaning $r_1 < 1$. All α, β, and ρ are positive, which means the four ratios are always positive. The fact that Lamé constants are always positive requires $\beta/\alpha \leq 1/\sqrt{2}$, which means $r_2 \leq 0.707$ and $r_3 < r_1$. This way all the square roots in eq. (3) are real numbers. To summarize these constraints,

$$0 < r_1 < 1 \quad , \tag{6a}$$

$$0 < r_2 \leq 0.707 \quad , \tag{6b}$$

$$0 < r_3 < r_1 < 1 \quad , \tag{6c}$$

and

$$0 < r_4 \ . \tag{6d}$$

Approximations to Zoeppritz

Although precise, eqs. (1) and (2) have often been considered to be too cumbersome for application, and various approximations have been derived and widely used in the conventional AVO analysis. Most practical applications are focused on the R_{PP}, thus in this subsection we only discuss the approximations to eq. (1). The most well-known approximations are the linearized versions (e.g., Aki and Richards, 1980; Shuey, 1985), for which Russell et al. (2011) give a comprehensive review. Desires for higher accuracy have been partly satisfied by the fourth-order Taylor expansion (see eq. (B-10) of Ursin and Dahl, 1992), the quadratic approximation [see eq. (10) of Wang, 1999], and the pseudo-linear approximation (see eq. (2) of Ursenbach, 2002). These

approximations are derived by assuming small contrasts and small angles and thus dropping higher-order terms in the Taylor expansion of eq. (1).

For the purpose of comparison, consider only the linear approximation (Aki and Richards, 1980; p. 153),

$$R_1(\bar{\theta}) = (\sec^2\bar{\theta}/2)(\Delta\alpha/\bar{\alpha}) - 4\sin^2\bar{\theta}(\bar{\beta}/\bar{\alpha})^2(\Delta\beta/\bar{\beta}) + [\tfrac{1}{2} - 2\sin^2\bar{\theta}(\bar{\beta}/\bar{\alpha})^2](\Delta\rho/\bar{\rho}) \quad . \tag{7}$$

and the quadratic approximation (Wang, 1999),

$$R_2(\bar{\theta}) = R_1(\bar{\theta}) + \cos\bar{\theta}\sin^2\bar{\theta}(\bar{\beta}/\bar{\alpha})^3[(\Delta\rho/\bar{\rho}) + 2(\Delta\beta/\bar{\beta})]^2 \quad . \tag{8}$$

In eqs. (7) and (8), $\bar{\theta}$ is the average of the incident and refracted angles,

$$\bar{\alpha} = (\alpha_2 + \alpha_1)/2, \quad \bar{\beta} = (\beta_2 + \beta_1)/2, \text{ and } \bar{\rho} = (\rho_2 + \rho_1)/2 \tag{9}$$

are the average elastic values across the interface, and

$$\Delta\alpha = (\alpha_2 - \alpha_1), \quad \Delta\beta = (\beta_2 - \beta_1), \text{ and } \Delta\rho = (\rho_2 - \rho_1) \tag{10}$$

are the elastic contrasts across the interface.

The Shuey's, quadratic, and pseudo-linear approximations are all based on eq. (7). Thus their parameterizations are the same. The RCs corresponding to the approximations

$$R_{aprx} = f[\bar{\theta},(\Delta\alpha/\bar{\alpha}),(\Delta\beta/\bar{\beta}),(\bar{\beta}/\bar{\alpha}),(\Delta\rho/\bar{\rho})] = f(\bar{\theta},\tilde{r}_1,\tilde{r}_2,\tilde{r}_3,\tilde{r}_4) \quad . \tag{11}$$

This classic parameterization [eq. (11)] is transformable from the ratio parameterization [eq. (5)], using

$$\tilde{r}_1/2 = (r_1 - 1)/(r_1 + 1), \quad \tilde{r}_2/2 = (r_3 - r_2)/(r_3 + r_2),$$
$$\tilde{r}_3 = (r_3 + r_2)/(r_1 + 1), \quad \tilde{r}_4/2 = (r_4 - 1)/(r_4 + 1), \tag{12}$$

as expected, as both are based on the six elastic parameters across the interface.

Numerical examples

The purpose of this section is to compare the accuracy of the Zoeppritz equation 1 and the approximate eqs. (7) and (8). To generate the "observed" AVA as a benchmark, we choose elastic finite-difference (FD) modeling. FD

solution of the heterogeneous wave equation with a point source simulates spherical waves and includes full-wave effects (Kelly et al., 1976). The well-known reflectivity method (e.g., Kennett, 1980) is not used because, as an integral method, its integration kernel contains the Zoeppritz RCs.

We use an eighth-order staggered-grid FD solution of the elastodynamic equations (Virieux, 1986), to produce the benchmark data for testing the inversions. The model has only two layers, and the values of (α_1, α_2, β_1, β_2, ρ_1, and ρ_2) are (5.72, 2.87, 2.93, 1.61, 2.86, and 2.14). The units for velocity and density are km/s and g/cm^3, respectively. These numbers are consistent with an anhydrite seal over a hydrocarbon-saturated sandstone reservoir (Martin et al., 2006). The velocities are decreasing from the upper to the lower layer, so there is no critical angle for either the PP or PS reflections. The explosive point source is a Ricker wavelet. The sources and receivers are in the upper layer and 1 km above the layer interface. The receivers record the (multi-component) vectors of particle velocity. The algorithm in Zhu et al. (2014a) is used to extract the benchmark AVA from the t-x domain seismogram data. The extracted amplitudes are corrected for geometrical spreading, and normalized by the amplitude of the source wavelet. The source normalization (Zhu and McMechan, 2014a) removes the source effects (including the frequency dependency), similar to a deconvolution.

Fig. 1 shows the PP/PS AVAs modeled by the FD, the Zoeppritz equations, and the linear and quadratic approximations, by crosses, red, green and blue lines, respectively. The red line fits the crosses closely, indicating that the Zoeppritz plane-wave RCs work well for the noncritical spherical-wave reflections. For this model (of such large contrasts), the linear approximation predicts higher amplitudes; the quadratic approximation is more precise at larger angles (as expected), but both are not as precise as the Zoeppritz equation. This is the main reason that we propose using the Zoeppritz equations for large (decreasing) velocity contrasts and large angles; it is theoretically correct for this case.

AVA INVERSION

System of linearized equations

From eq. (5), a maximum of four parameters can be estimated from the plane-wave RCs (Ursin and Tjåland, 1996). They are the three velocity ratios (r_1, r_2, r_3) and one density ratio (r_4), as further defined in eqs. (4). Our inversion aims to invert for all the four ratios. It is currently common practice to derive rock properties from the old model parameterization [eq. (11)], which can be easily derived from the four ratios [eq. (12)]; if one has confidence in the α_1 and ρ_1 values, then α_2, β_1, β_2 and ρ_2 can also be derived from the four ratios.

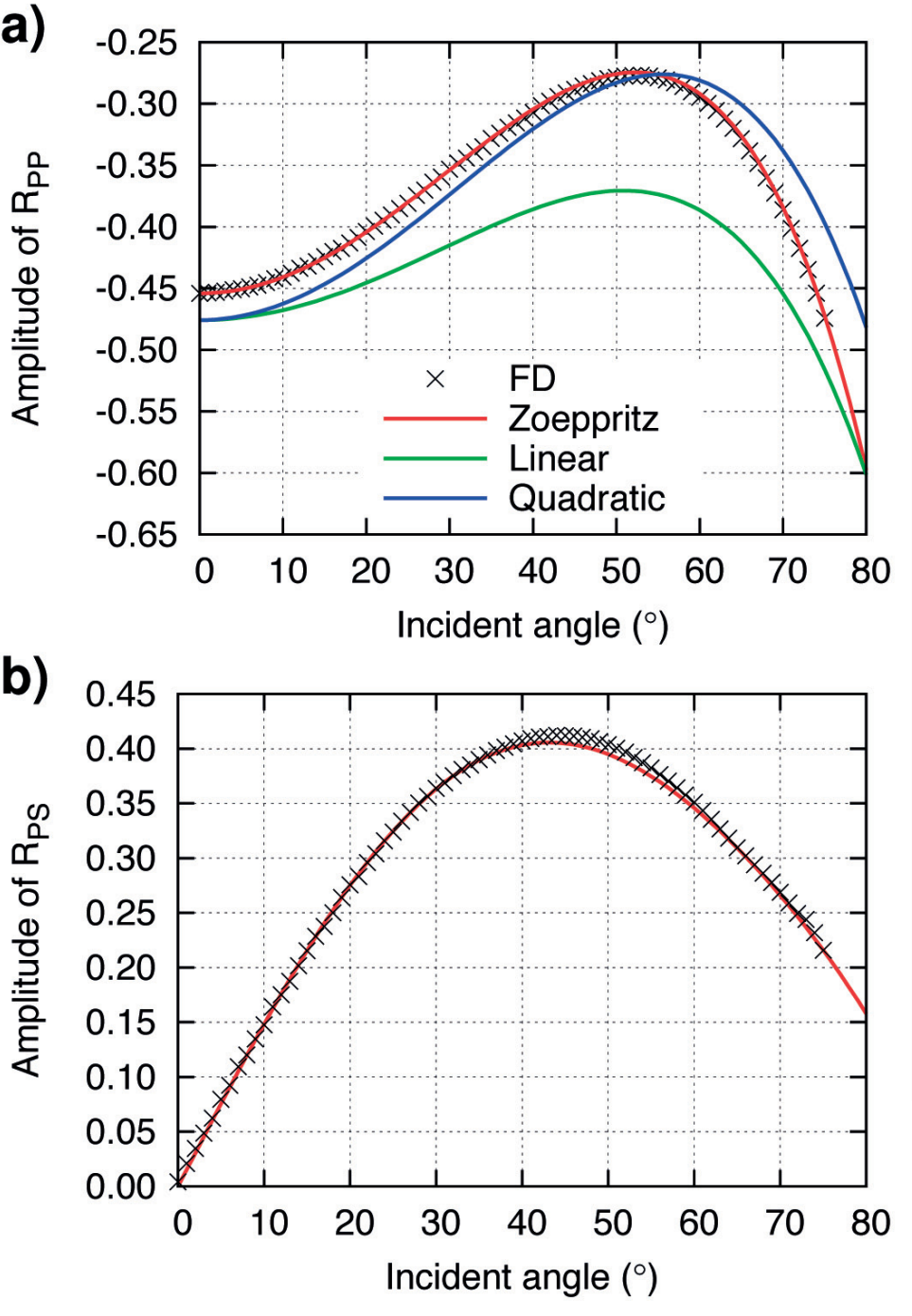

Fig. 1. AVAs of R_{PP} (a) and R_{PS} (b) from different modeling methods. The red, green, and blue lines are from the Zoeppritz equations, and the linear and quadratic approximations, respectively. The crosses are the benchmark from the FD method.

The inversion solves the system of linearized equations

$$\mathbf{A}_{m\times n}\,\mathbf{x}_n = \mathbf{b}_m \quad , \tag{13}$$

where n = 4 is the number of unknowns (the parameter ratios), and m is the number of AVA data points. The **x** is the model (ratio) update vector, and **b** contains the differences between the predicted and observed AVA data. The (synthetic) predicted AVA are modeled by the Zoeppritz equations, and the observed AVA should be corrected for polarization, spreading, attenuation, transmission losses, etc. In this paper, we use the FD benchmark AVAs (the crosses in Fig. 1) as the observed AVA. **A** is the Jacobian matrix containing the Fréchet derivatives, which are calculated analytically (see the following section).

To make the system over-determined, the number of independent data must be $m \geq 4$. Then we use least squares to solve the system [eq. (13)] for the model updates. After the model is updated, it is used as the starting model for the next iteration. Iteration proceeds until convergence is reached, by the criterion that the norm of data residual vector **b** cannot be reduced, or that the norm of model update vector **x** is below a threshold value.

Fréchet derivatives

Wang (1999) notes that an immediate advantage of using the approximations, rather than the Zoeppritz equations, is that the sensitivity matrix of Fréchet derivatives of amplitudes with respect to elastic parameters can be computed analytically from eqs. (7) or (8); it is not necessary to compute these numerically. However, since the Zoeppritz R_{PP} and R_{PS} have explicit expressions [eqs. (1) and (2)], their Fréchet derivatives can also be derived analytically. We use the symbolic manipulation tool in Mathematica© for this task (Zhu and McMechan, 2012a).

Appendix A contains the Mathematica© script, and Appendix B contains representative results for the analytic Fréchet derivatives of R_{PP} with respect to r_1, r_2, r_3, and r_4. These are straightforward to use after coded to computer programs. To illustrate, we use the same elastic model as in the modeling section: (α_1, α_2, β_1, β_2, ρ_1, and ρ_2) are (5.72, 2.87, 2.93, 1.61, 2.86, and 2.14). The actual input parameters to the equations are the four unitless ratios (r_1, r_2, r_3, and r_4) set to (0.502, 0.512, 0.281, and 0.748), according to eq. (4). All the examples in this paper use this as the true model, thus it is not repeated in the following sections. Figs. 2 and 3 show the analytic derivatives of R_{PP} and R_{PS}, at incident angles of 10°, 30°, and 50°, by red, green, and blue lines, respectively. We cross-check the analytic equations by also calculating the derivatives numerically, by the three-step procedure of model perturbation, Zoeppritz modeling, and differentiation. The squares, circles, and triangles in

Figs. 2 and 3 are calculated numerically at 10°, 30°, and 50° incident angles. The overlap of the points and lines validates both approaches. For both R_{PP} and R_{PS}, the three velocity ratios (r_1, r_2, r_3) generally have higher derivatives at larger incident angles, which means that the AVA curves have larger gradients, or sensitivities to the elastic parameter ratios at larger angles.

In numerical calculation of the derivatives, an optimal parameter perturbation needs to be decided. It needs to be small enough for the differentiation to capture the local gradient,but not so small as to cause round-off errors. The perturbation used is 0.001 for all four ratios. The analytic method, of course, does not have this issue.

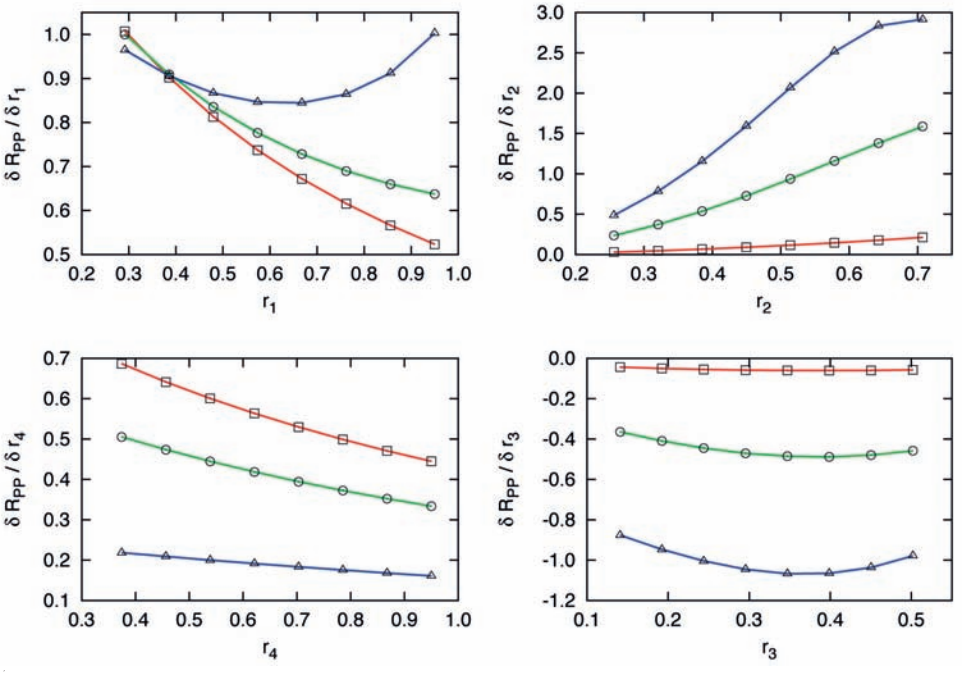

Fig. 2. Fréchet derivatives of R_{PP} with respect to the four ratios. The red, green, and blue lines are analytically calculated at incident angles of 10°, 30°, and 50°, respectively. The squares, circles, and triangles are numerically calculated at 10°, 30°, and 50° incident angles.

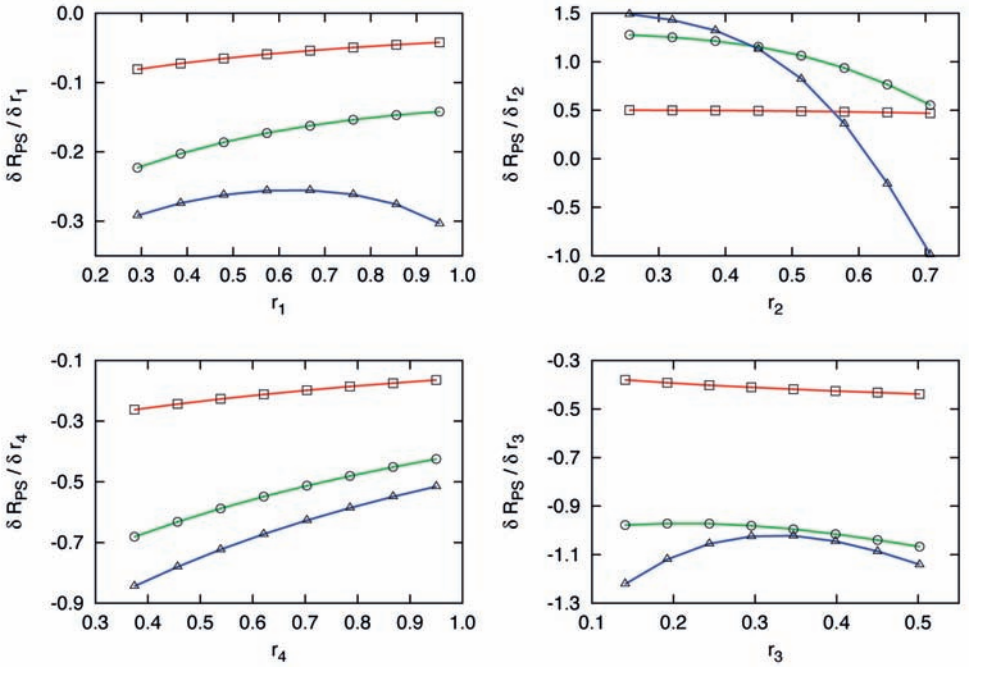

Fig. 3. Fréchet derivatives of R_{PS} with respect to the four ratios. The red, green, and blue lines are analytically calculated at incident angles of 10°, 30°, and 50°, respectively. The squares, circles, and triangles are numerically calculated at 10°, 30°, and 50° incident angles.

Condition number

The condition number is a property of the Jacobian matrix (**A**) in eq. (13). It is defined as the ratio of the largest to smallest eigenvalues [if **A** is a square matrix (i.e., m = n)] or the ratio of the largest to smallest singular values [if A is nonsquare (i.e., m ≠ n)]. The system is typically over-determined (m > n), so we use singular value decomposition (SVD) to calculate the condition number. If the condition number is high, the system is ill-conditioned, which means that a small error in **b** may cause a large error in **x**. If the condition number is low, the system is well-conditioned and the error in **x** will not be much larger than the error in **b**.

To build the Jacobian matrix **A**, we define a maximum available incident angle θ_m, and set the number of incident angles m = 10. The 10 angles are sampled uniformly from 1° to θ_m. The number of unknowns is four (n = 4), so the dimension of **A** is 10 × 4 if only R_{PP} is considered. The elements of **A** (i.e., the Fréchet derivatives) are calculated analytically. The condition number of A

is then calculated by SVD. Repeating this procedure for different θ_m gives the solid line in Fig. 4. If we use jointly R_{PP} and R_{PS}, each angle has two data points so the dimension of **A** becomes 20 × 4; the dashed line in Fig. 4 corresponds to this scenario. The condition number is much smaller when PP and PS data are combined.

The oscillation of the solid line at $\theta_m < 15°$ is mainly because the smallest singular values are very small and oscillating, which indicates that it is highly ill-conditioned to invert for the 4 ratios using R_{PP} only at such narrow angles. For both the solid and dashed lines, the condition number decreases with increasing θ_m, which indicates a wider angle aperture stabilizes the inversion system. We use a constant number of angles ($m = 10$) in all angle apertures. As long as the system is over-determined ($m \geq n$), the factor that matters is not simply the number of angles, but the angle aperture, which in turn indicates the independence of the information in the data. R_{PS} is another kind of independent data, which, after being added to the system, reduces the condition number by more than half (Fig. 4).

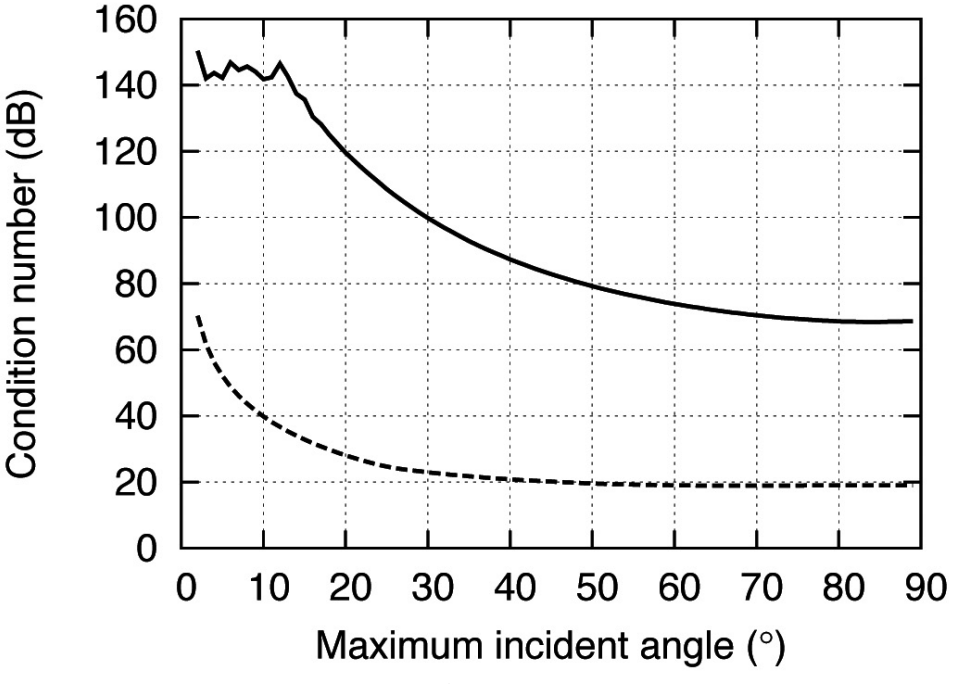

Fig. 4. The condition numbers of the Jacobian matrices. The solid line is for using R_{PP} alone, and the dashed line is for using R_{PP} and R_{PS} jointly.

Besides increasing the number of independent data (m), another way to improve the conditioning is to reduce the number of unknowns (n). Examples include using the linear approximation to invert for only two elastic parameters (usually the impedances $\bar{\alpha}\bar{\rho}$ and $\bar{\beta}\bar{\rho}$), or using the quadratic approximation to invert for only three parameters (i.e., $\Delta\alpha/\bar{\alpha}$, $\Delta\beta/\bar{\beta}$, $\bar{\beta}/\bar{\alpha}$), by assuming the third and/or fourth parameters known a priori (Wang, 1999). These constraints may come from different (independent) data types (e.g., well, lab, or lithology).

Inversion examples

As outlined above, we propose using the Zoeppritz equations and their analytic Fréchet derivatives to do linearized iterative AVA inversion. First, we compare PP inversions by Zoeppritz and by its approximations. Then, we show numerical examples of inverting PP alone and PP/PS jointly, to explore the effects of starting models, angle ranges, and noise. The constraints [eq. (6)] are applied at each iteration of the inversions using the Zoeppritz equations.

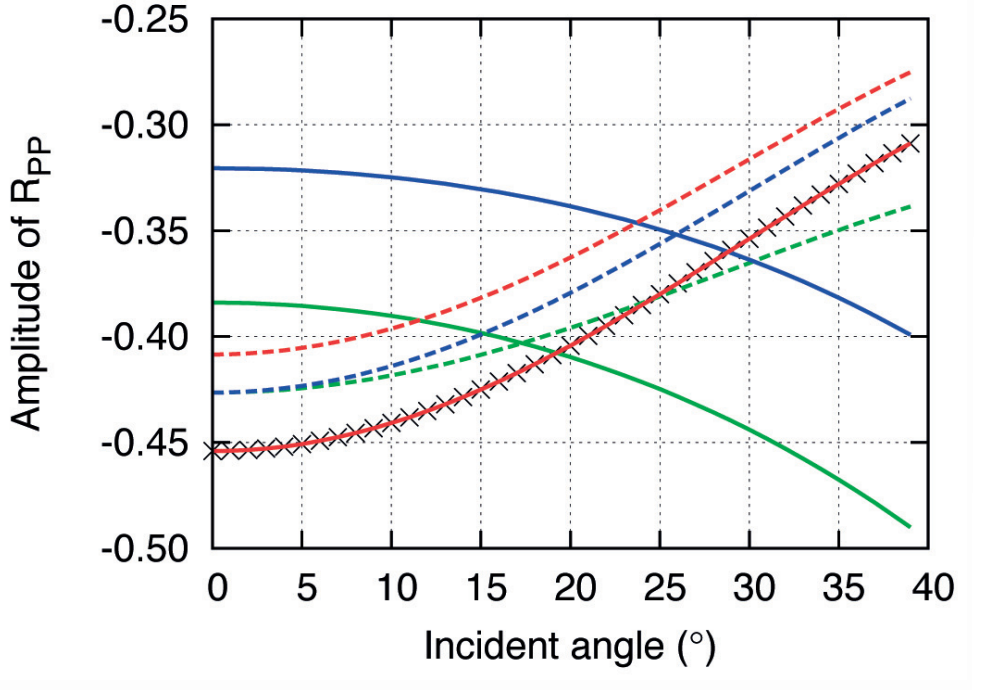

Fig. 5. AVAs of the PP RCs. The crosses are the observed AVA from FD modeling. The dashed and solid lines are predicted AVAs from the starting and inverted models, respectively. The red, green, and blue lines are for the Zoeppritz equation, and the linear and quadratic approximations, respectively.

Zoeppritz vs. approximations

We compare PP inversions of using the Zoeppritz eq. (1), the linear approximation [eq. (7)], and the quadratic approximation [eq. (8)]. The inversion system is the same for all three; the only difference is that the Zoeppritz inverts for (r_1, r_2, r_3, and r_4), while the approximations invert for ($\bar{r}_1, \bar{r}_2, \bar{r}_3$, and $\bar{r}_4$). The Fréchet derivatives of the approximations are easily derived from eqs. (7) and (8).

The crosses from FD modeling (in Fig. 1) are used as the observed AVA. We choose a starting model close to the true model: (r_1, r_2, r_3, and r_4) are (0.6, 0.5, 0.3, and 0.7), or equivalently ($\tilde{r}_1$, $\tilde{r}_2$, $\tilde{r}_3$, and $\tilde{r}_4$) are (-0.5, -0.5, 0.5, and -0.353). The incident angles used are from 0° to 40° sampled every 1°. Fig. 5 shows the AVAs of the PP RCs. The crosses are the observed AVA (the same as in Fig. 1). The dashed and solid lines are predicted AVAs from the starting and inverted (at the 50th iteration) models, respectively. The red, green, and blue lines are for the Zoeppritz equation, and the linear and quadratic approximations, respectively. Fig. 6 shows the relative errors of the inverted ratios, and Fig. 7 shows the total data residual errors.

From Fig. 7, both inversions using approximations are diverging, which is confirmed by the ratios in Fig. 6. After 100 iterations (not shown), the divergence continues. This demonstrates that the linear and quadratic approximations are incapable of inverting for four parameters. With the same angle range, the Zoeppritz inversion, in contrast, converges to the true model within 6 iterations and stays there (Figs. 6c and 7). This demonstrates the superiority of inversion using Zoeppritz to those using approximations; thus, for the rest of the examples below, we do only Zoeppritz-based inversions.

Starting model test

In the previous example, we use a starting model close to the true model. In this example, we test two starting models farther from the true model. We compare inversions using PP alone and PP/PS jointly. The joint PP/PS inversion has the same inversion system as PP-alone inversion, except the number of data (m) is twice that of the latter, by adding the PS AVAs.

Fig. 8 shows the inversion results with the starting ratios (0.753, 0.768, 0.422, and 1.122) deviated from the true ratios by 50%. The incident angles used are from 0° to 50° sampled every 1°. Both inversions (PP alone and PP/PS jointly) converge to the true model within 20 iterations, while the convergence path of the joint inversion is a little shorter.

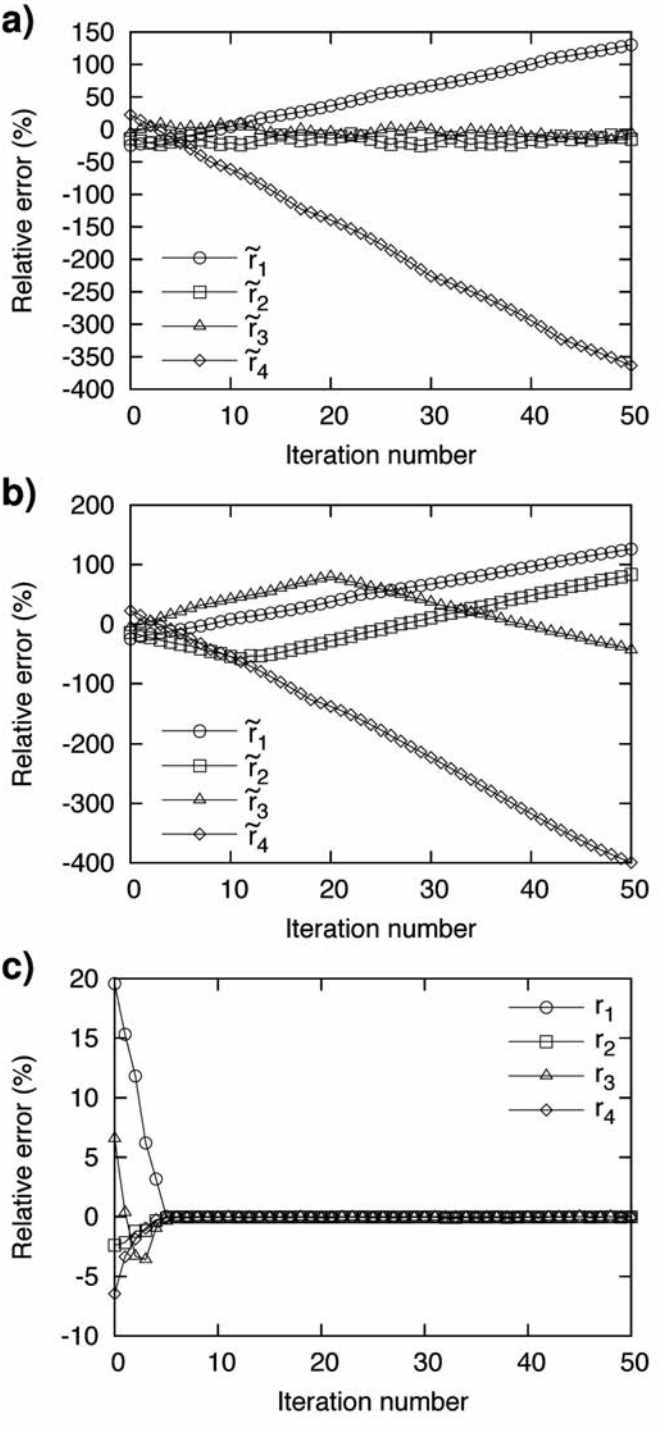

Fig. 6. The updated ratios at each iteration. PP inversion (a) uses the linear approximation, (b) uses the quadratic approximation, and (c) uses the Zoeppritz equation.

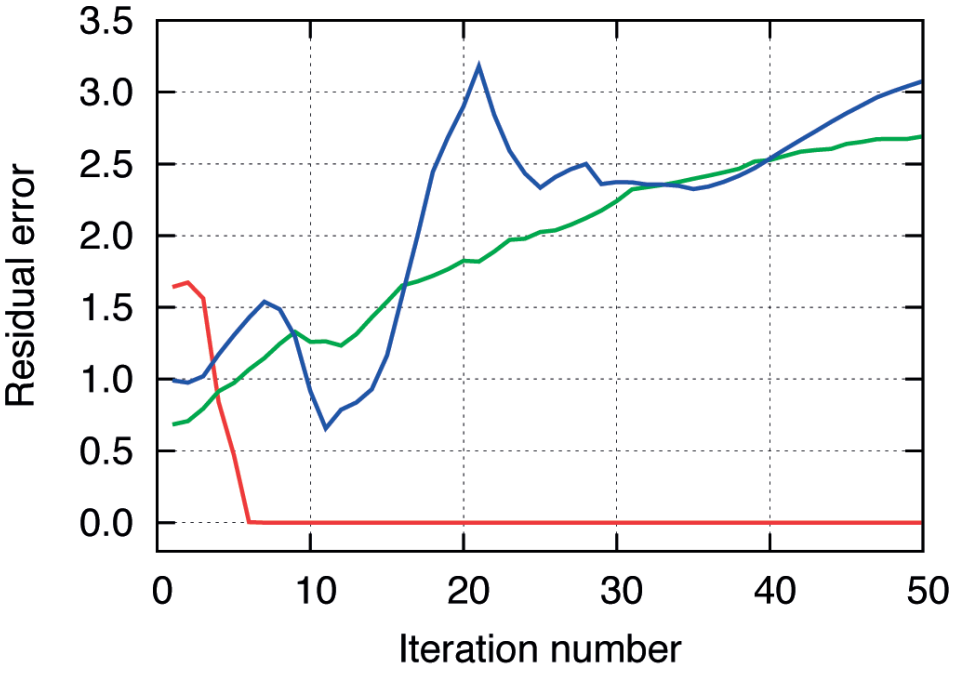

Fig. 7. Total data residual errors at each iteration. The red, green, and blue lines are for inversions using the Zoeppritz PP equation, and its linear and quadratic approximations, respectively.

Fig. 9 shows the inversion results with the starting ratios (0.99, 0.50, 0.50, and 1.00). In this starting model, $r_1 = 0.99$ means almost no V_P contrast. The $r_2 = 0.5$ means the $\beta_1/\alpha_1 = 0.5$ which is a typical value in sedimentary rocks. The $r_3 = r_2$ means no V_S contrast, and the $r_4 = 1.0$ means no density contrast. The incident angles used are from 0° to 70° sampled every 1°. From the same starting model, the inversion using PP data alone (Fig. 9a) falls into a local minimum, while the joint PP/PS inversion (Fig. 9b) converges to the true model at about 23 iterations.

Angle range test

Next we test the effects of the incident angle range on the inversion. In Fig. 10, one maximum incident angle (θ_m) corresponds to one inversion result at the 50th iteration. The incident angles used in each inversion are from 0° to θ_m sampled every 1°. The starting ratios (0.753, 0.768, 0.422, and 1.122) deviate from the true ratios by 50%. For the relative errors to converge to zeros, the PP-alone inversion (Fig. 10a) needs a angle range larger than 25°,

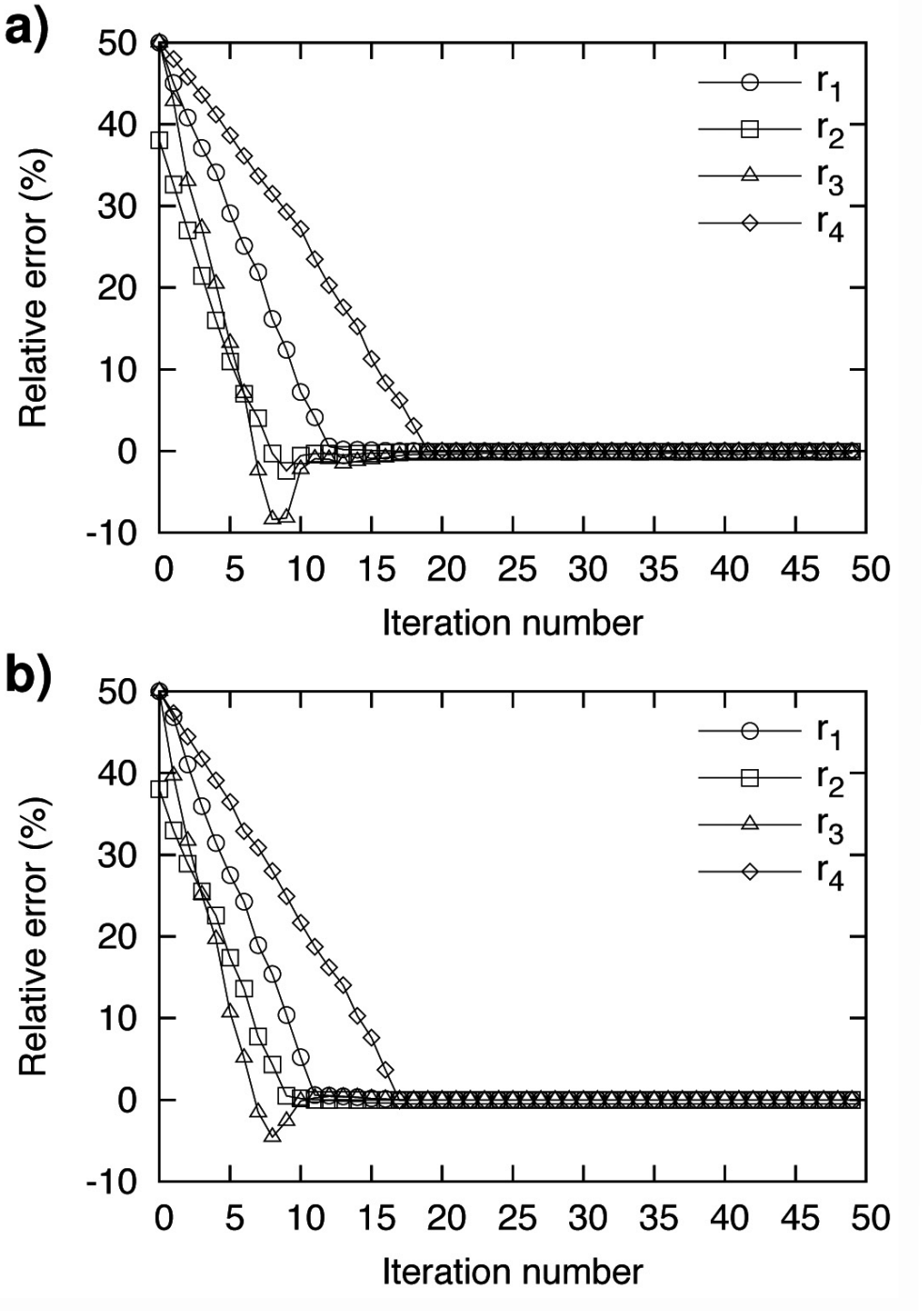

Fig. 8. Relative ratio errors as a function of iteration. The starting ratios (0.753, 0.768, 0.422, and 1.122) deviate from the true ratios (0.502, 0.512, 0.281, and 0.748) by 50%. (a) uses PP data alone, and (b) uses PP and PS data jointly.

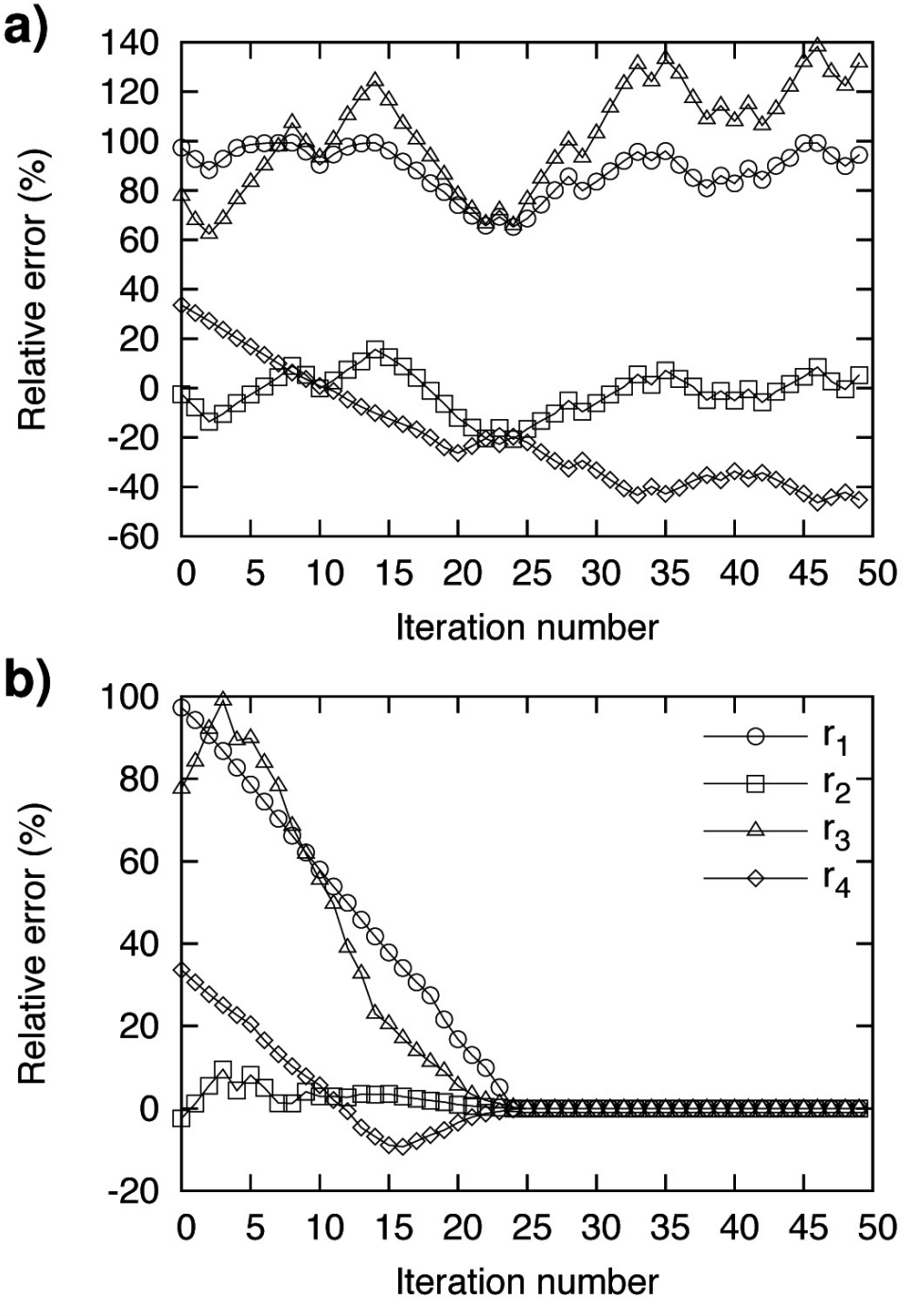

Fig. 9. Relative ratio errors as a function of iteration. The starting ratios (r_1, r_2, r_3 and r_4) are (0.99, 0.50, 0.50, are 1.00), and the true ratios are (0.502, 0.512, 0.281, are 0.748). (a) uses PP data alone, and (b) uses PP and PS data jointly.

while the joint inversion (Fig. 10b) converges all four ratios to very small relative errors (less than $\pm 0.06\%$) even with $\theta_m = 4°$, i.e., data at four angles of 0°, 1°, 2°,and 3°. In Fig. 11, everything is the same as in Fig. 10, except that the starting ratios are (0.99, 0.50, 0.50, and 1.00). The PP-alone inversion (Fig. 11a) falls into local minima, while the joint inversion (Fig. 11b) converges all four relative errors to less than $\pm 0.09\%$ even with $\theta_m = 4°$. In both Figs. 10b and 11b, all four relative errors are reduced to near zeros if the angle apertures are wider than 12°.

Every linearized inversion (of a nonlinear problem) suffers the issue of local minima, and thus requires that the starting model be "sufficiently close" to the global minimum or the true model. For a given starting model, Fig. 10a demonstrates that a wider angle range (more independent data) can help reduce the local minima. However, the inversion may still fail even with ultra wide angle ranges, if we use PP data alone (as in Fig. 11a). In contrast, the joint inversion (Fig. 11b) works surprisingly well even with a very narrow angle range. The robustness of the joint PP/PS inversion is much higher than that of PP-alone inversion; this is consistent with Zhi et al. (2013). We have done similar tests with many other true models (not shown); all the results support the same conclusions.

Random noise test

We add some random noise to the benchmark AVA from FD modeling (the crosses in Fig. 1), as the observed data (the pluses in Fig. 12). We test the joint PP/PS inversion using Zoeppritz equations. The starting ratios are (0.99, 0.50, 0.50, and 1.00). The incident angle apertures used range from 20° to 70° with observations spaced every 1°.The AVAs corresponding to the inverted ratios are shown as red solid lines in Fig. 12, which exhibit good least-squares fitting to the noisy observed data. The residual errors of the four ratios are reduced from (97.31%, −2.39%, 77.64%, and 33.64%) to (0.55%, 1.24%, 4.84%, and −2.35%); the remaining errors are caused by the biased observed data (the pluses in Fig. 12), because the noise added are not perfectly random. The green, blue, and purple lines in Fig. 12 correspond to the same experiment but using angle apertures of 60°, 40°, and 20°. It is obvious that a wider angle aperture can also compensate for noise in the data. Coherent noise such as multiples or P-S converted waves, or waves produced by cultural sources, may contaminate the observations where they overlap in time and space with the target data. This overlap will be more detrimental where the slowness of the noise is also close to that of the target reflection. However, the data for each reflection point are in common-reflection-point gathers, so each trace is from a different source and receiver pair,which reduces the probability of unaliased coherence over large offset apertures. Local interference will affect only the local data.

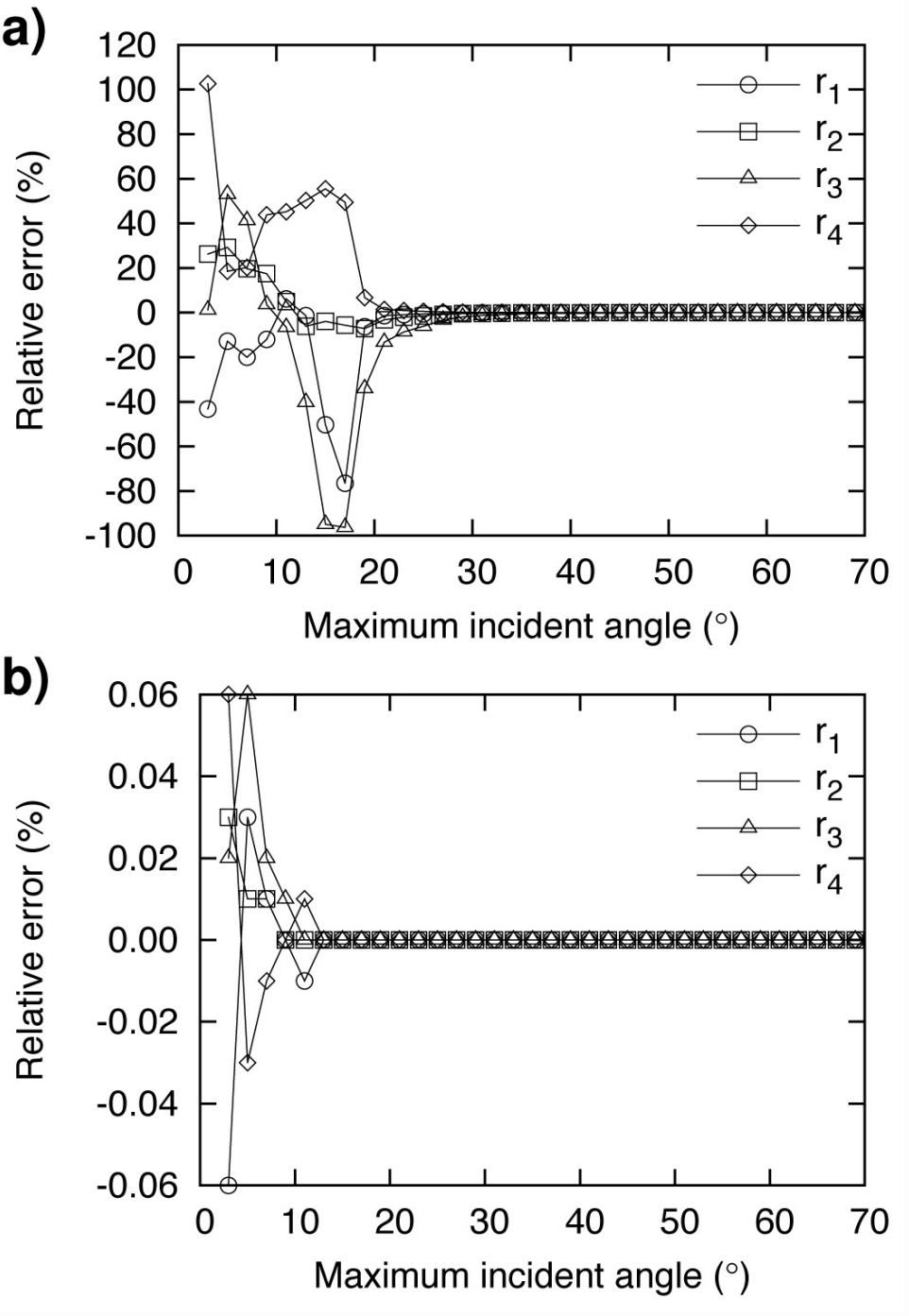

Fig. 10. Relative ratio errors as a function of angle range. The starting ratios (0.753, 0.768, 0.422, and 1.122) deviate from the true ratios (0.502, 0.512, 0.281, and 0.748) by 50%. (a) uses PP data alone, and (b) uses PP and PS data jointly.

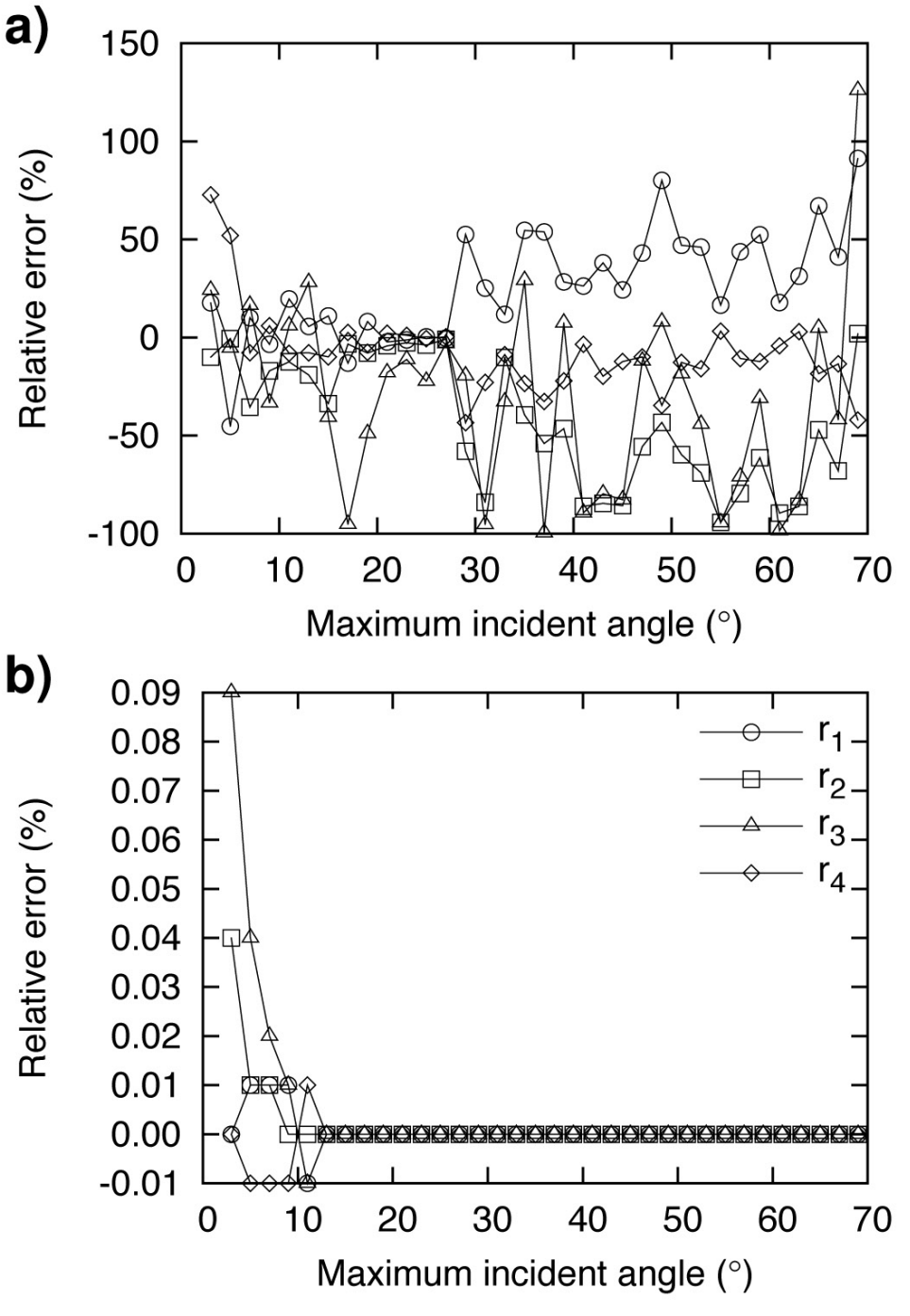

Fig. 11. Relative ratio errors as a function of angle range. The starting ratios (r_1, r_2, r_3 and r_4) are (0.99, 0.50, 0.50, and 1.00), and the true ratios are (0.502, 0.512, 0.281, and 0.748). (a) uses PP data alone, and (b) uses PP and PS data jointly.

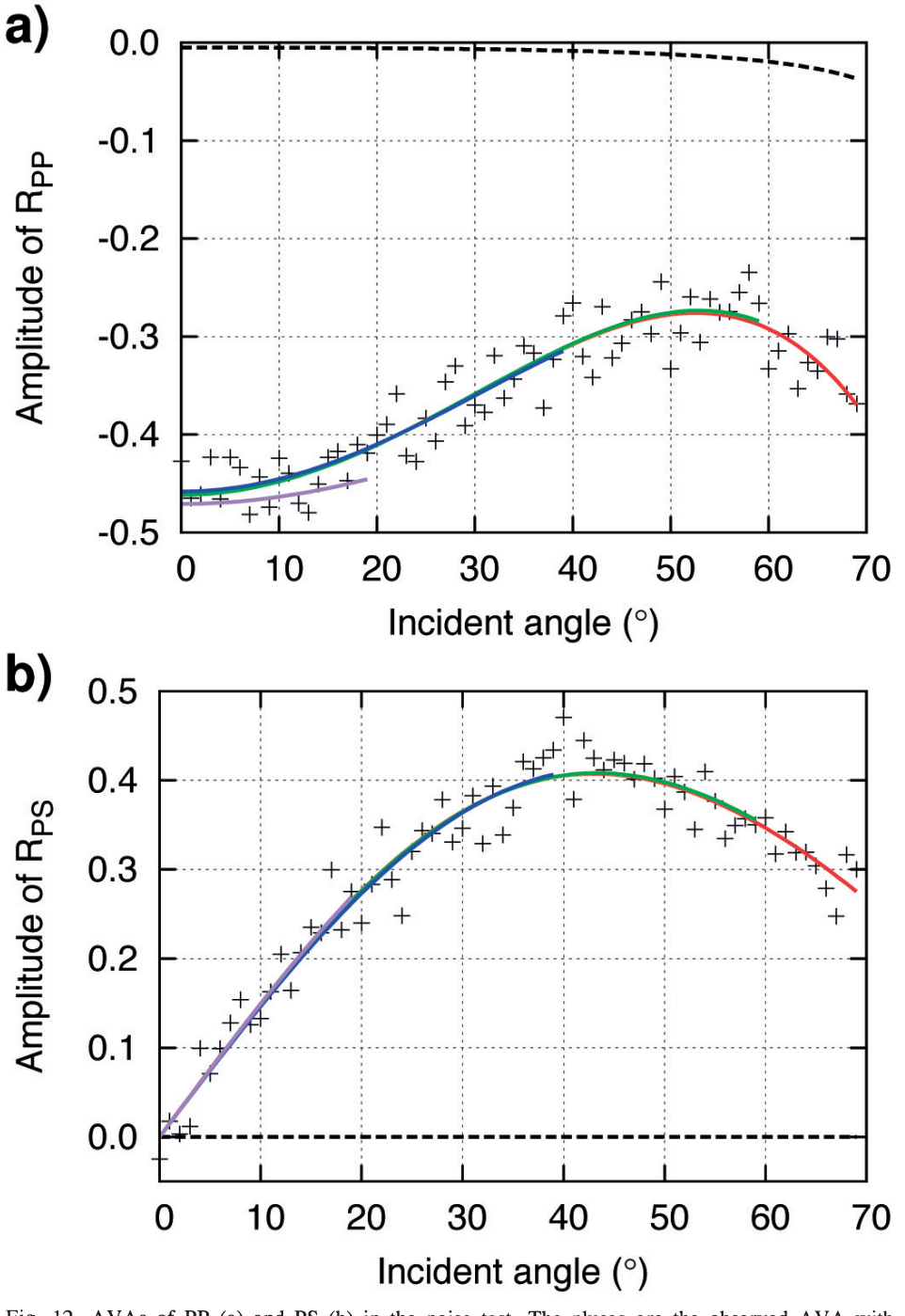

Fig. 12. AVAs of PP (a) and PS (b) in the noise test. The pluses are the observed AVA with random noise. The dashed lines are the AVAs from the starting ratios (0.99, 0.50, 0.50, and 1.00), and the solid lines are from the inverted ratios. The red, green, blue, and purple colors correspond to using angle apertures of 70°, 60°, 40°, and 20°. Compare with the correct solution in Fig. 1.

DISCUSSION

We assume no critical angle ($r_1 < 1$) at the target reflector, so the analytic Fréchet derivatives are derived knowing that all the square roots in eq. (3) are real and thus that the R_{PP} and R_{PS} are real, and there is no phase variation with angle (PVA). Such interfaces of decreasing V_P (or $r_1 < 1$) are not uncommon in hydrocarbon exploration. Examples include over-pressure zones and reservoirs (such as gas sand) trapped beneath tight carbonates, salts, or volcanics (which all have high V_P). The underlying reservoir rocks have lower V_P because of their porosity and fluid saturation.

What if the target does have a critical angle? As they assume plane waves, the Zoeppritz RCs fail near the critical angle. If the angle range considered is below the first Fresnel zone of the critical angle, the algorithm may still be applied. For near- and post-critical angles, one option is to use spherical-wave RCs (Skopintseva et al., 2011; Zhu and McMechan, 2012b). Another option is to decompose the spherical wavefield into plane waves (e.g., by the τ-p transform) and still use the Zoeppritz RCs (Zhu and McMechan, 2014).

Now compare the Zoeppritz equations and the consequences of their approximations. At large angles (excluding the neighborhood of the critical angle), in models with large velocity or density contrasts, the approximations to the Zoeppritz equations break down, while the Zoeppritz equations are analytically accurate. If approximations give AVA sufficiently close to that of the Zoeppritz RCs, they can be used in inversion; if not, the Zoeppritz equations have to be used [instead of the approximations (Figs. 5, 6, and 7)].

Russell et al. (2011) give two arguments for AVA using linearized approximations rather than the Zoeppritz equations; these provide an intuitive understanding of the amplitude effects of the parameter changes, and instability of nonlinear inversion by the Zoeppritz equation. Linearizing the nonlinear Zoeppritz equation does provide simpler (and thus, easier) algebra, but at the cost of accuracy (Fig. 1). We have shown that Zoeppritz modeling can be integrated into a linearized inversion system and good stability is achieved.

Wang (1999) argues that analytic Fréchet derivatives are available for approximations. We have shown that Fréchet derivatives can also be analytically calculated from the Zoeppritz equations, by using symbolic manipulation software to overcome the complexity of the algebra. The same strategy can be applied to SS and SP reflections, thus the full elastic wavefield can be exploited.

Various parameterizations (besides eq. (11)] have been developed in conventional AVA analysis, including the use of Poisson's ratio and impedance contrasts. Different parameterizations have different AVA sensitivities. Our

algorithm uses the ratios [eq. (5)], for which the Fréchet derivatives are available analytically. Besides, the ratios are more natural and intuitive than the parameterization in eq. (11) which mixes the parameters across the interface.

The analytic accuracy of Zoeppritz RCs enables inclusion of larger angles and to invert for four parameters, compared to conventional two- and three-term AVO inversions. The four-parameter inversion may fall into a local minimum if we use PP alone and the starting model is far from the true model. Wider angle ranges of PP help but not as much as using the joint PP/PS data. Numerical tests show that the joint PP/PS can reliably invert all four ratios from PP/PS data with a narrow angle range and a starting model that is far from the correct one (Figs. 10b and 11b). Long-offset surveys are preferred in that they provide wide-angle apertures thus more independent AVA data constraints. For even more robust AVA inversion, we recommend acquiring PS reflections with multi-component receivers and longer recording times (than if we only acquire PP reflections). The observed AVA can be extracted from either the data domain (Zhu and McMechan, 2014), or the image domain via true-amplitude prestack migration (Arntsen et al., 2013).

CONCLUSIONS

We propose a new AVA algorithm by using the Zoeppritz equations, rather than the various approximations, for target-oriented inversion of reservoirs whose velocities decrease at their tops. We use a parameterization in terms of elastic parameter ratios, calculate the Fréchet derivatives analytically, and solve the linearized system by least-squares. With this algorithm, we can invert for four ratios with PP data alone; the joint PP/PS inversion can reliably invert four ratios from data within a relatively narrow angle range and with a starting model that is far from the correct model. A wider angle aperture is necessary to offset noise in the data. This algorithm is particularly useful for target-oriented AVA inversion of long-offset multi-component seismic data.

ACKNOWLEDGEMENTS

The research leading to this paper is supported by the Sponsors of the UT-Dallas Geophysical Consortium. This paper is Contribution No. 1260 from the Department of Geosciences at the University of Texas at Dallas.

REFERENCES

Aki, K.T. and Richards, P.G., 1980. Quantitative Seismology: Theory and Methods, W.H. Freeman, San Francisco.

Alhussain, M., Gurevich B. and Urosevic, M., 2008. Experimental verification of spherical wave effect on the AVO response and implications for three-term inversion. Geophysics, 73(2): C7-C12.

Arntsen, B., Kritski, A., Ursin, B. and Amundsen, L., 2013. Shot-profile true amplitude crosscorrelation imaging condition. Geophysics, 78(4): S221-S231.

Beaudoin, G., 2010. Imaging the invisible - BP's path to OBS nodes. Expanded Abstr., 80th Ann. Internat. SEG Mtg., Denver: 3734-3739.

Bortfeld, R., 1961. Approximation to the reflection and transmission coefficients of plane longitudinal and transverse waves. Geophys. Prosp., 9: 482-502.

Červený, V., Molotkov, I.A. and Pšenčík, 1977. Ray Method in Seismology. Charles University Press, Prague.

Coleman, T.F. and Li, Y., 1994. On the convergence of interior-reflective Newton methods for nonlinear minimization subject to bounds. Mathemat. Program., 67: 189-224.

Deng, F. and McMechan, G.A., 2007. True-amplitude prestack depth migration, Geophysics, 72(3): S155-S166.

Kelly, K.R., Ward, R.W., Treitel, S. and Alford, R.M., 1976. Synthetic seismograms: A finite-difference approach. Geophysics, 41: 2-27.

Kennett, B.L.N., 1981. Seismic waves in a stratified half space - II. Theoretical seismograms. Geophys. J. Roy. Astron. Soc., 61: 1-10.

Lehocki, I., Avseth, P. and Veggeland, T., 2013. Exact Zoeppritz-inversion of Vp/Vs ratio - application to a Barents Sea gas reservoir. Extended Abstr., 75th EAGE Conf., London: Th P15 05.

Ma, J., Fu, G.P., Geng, J. and Guo, T.L., 2013. Full Zoeppritz equation-based elastic parameters Bayesian generalized linear inversion. Extended Abstr., 75th EAGE Conf., London: Tu 10 14.

Martin, G.S., Wiley, R. and Marfurt, K.J., 2006. Marmousi2: An elastic upgrade for Marmousi. The Leading Edge, 25: 156-166.

Moldoveanu, N., Ji, Y. and Beasley, C., 2012. Multivessel coil shooting acquisition with simultaneous sources. Expanded Abstr., 82nd Ann. Internat. SEG Mtg., Las Vegas, doi:10.1190/segam2012-1526.1

Russell, B.R., Gray, D. and Hampson, D.P., 2012. Linearized AVO and poroelasticity. Geophysics, 76(3): C19-C29.

Shuey, R.T., 1985. A simplification of the Zoeppritz equations. Geophysics, 50: 609-614.

Skopintseva, L., Ayzenberg, M., Landrø, M., Nefedkina, T. and Aizenberg, A.M., 2011. Long-offset AVO inversion of PP reflections from plane interfaces using effective reflection coefficients. Geophysics, 76: C65-C79.

Ursenbach, C.P., 2002. Optimal Zoeppritz approximations. Expanded Abstr., 72nd Ann. Internat. SEG Mtg., Salt Lake City: 1897-1900.

Ursin, B. and Dahl, T., 1992. Seismic reflection amplitudes. Geophys. Prosp., 40: 483-512.

Ursin, B. and Tjåland, E., 1996. The information content of the elastic reflection matrix. Geophys. J. Internat., 125: 214-228.

Virieux, J., 1986. P-SV wave propagation in heterogeneous media: velocity-stress finite difference method. Geophysics, 51: 889-901.

Wang, Y., 1999. Approximation to the Zeoppritz equations and their use in AVO analysis. Geophysics, 64: 1920-1927.

Zhi, L., Chen, S. and Li, X., 2013. Joint AVO inversion of PP and PS waves using exact Zoeppritz equation. Expanded Abstr., 83rd Ann. Internat. SEG Mtg., Houston: 457-461.

Zhu, X. and McMechan, G.A., 2012a. AVO inversion using the Zoeppritz equation for PP reflections. Expanded Abstr., 82nd Ann. Internat. SEG Mtg., Las Vegas. doi:10.1190/segam2012-0160.1

Zhu, X. and McMechan, G.A., 2012b. Elastic inversion of near- and post-critical reflections using phase variation with angle. Geophysics, 77(4): R149-R159.

Zhu, X. and McMechan, G.A., 2014. Amplitude and phase versus angle for elastic wide-angle reflections in the τ-p domain. Geophysics, 79(4): submitted.

APPENDIX A

SCRIPT TO DERIVE THE FRÉCHET DERIVATIVES

Mathematica© provides a symbolic manipulation tool. Running the following script in Mathematica gives analytic expressions of the Fréchet derivatives of the exact Zoeppritz equations for PP and PS reflections. Appendix B contains the derivatives of PP with respect to r_1, r_2, r_3 and r_4.

```
Q = 2*Sin[theta]^2*(r4*r3^2-r2^2)
T0 = Tan[theta]
T1 = r1*Sin[theta]/Sqrt[1-r1^2*Sin[theta]^2]
T2 = r2*Sin[theta]/Sqrt[1-r2^2*Sin[theta]^2]
T3 = r3*Sin[theta]/Sqrt[1-r3^2*Sin[theta]^2]
F1 = Q^2+r4*T1*T2+(r4-Q)^2*T1*T3
F2 = r4*T0*T3+(1+Q)^2*T0*T2+(r4-Q-1)^2*T0*T1*T2*T3
F3 = 2/r2*T2*(Q*(1+Q)+(r4-Q)*(r4-Q-1)*T1*T3)
Rpp = (F1-F2)/(F1+F2)
Rps = F3/(F1+F2)
Dt[Rpp,r1,Constant->{r2,r3,r4,theta}]
Dt[Rpp,r2,Constant->{r1,r3,r4,theta}]
Dt[Rpp,r3,Constant->{r1,r2,r4,theta}]
Dt[Rpp,r4,Constant->{r1,r2,r3,theta}]
Dt[Rps,r1,Constant->{r2,r3,r4,theta}]
Dt[Rps,r2,Constant->{r1,r3,r4,theta}]
Dt[Rps,r3,Constant->{r1,r2,r4,theta}]
Dt[Rps,r4,Constant->{r1,r2,r3,theta}]
```

APPENDIX B

CALCULATION OF THE FRÉCHET DERIVATIVES

This Appendix contains the Fortran codes for the four representative Fréchet derivatives of R_{PP} with respect to r_1, r_2, r_3 and r_4.

This is the Fortran code to calculate the Fréchet derivative of R_{PP} with respect to r_1.

```
c1 = ( 1 + Q )**2
c2 = ( r4 - Q )**2
c3 = ( r4 - Q - 1 )**2
d1 = r4 / r1 * T1**3 * T2
d2 = r4 / r1 * T1 * T2
d3 = c2 / r1 * T1**3 * T3
d4 = c2 / r1 * T1 * T3
d5 = c3 / r1 * T0 * T1**3 * T2 * T3
d6 = c3 / r1 * T0 * T1 * T2 * T3
d7 = Q**2 + r4 * T1 * T2
d8 = c2 * T1 * T3 - r4 * T0 * T3
d9 = - c3 * T0 * T1 * T2 * T3
d10 = - c1 * T0 * T2
d11 = c2 * T1 * T3 + r4 * T0 * T3
e1 = d1 + d2 + d3 + d4 + d5 + d6
e2 = d7 + d8 + d9 + d10
e3 = d7 + d11 - d9 - d10
e4 = d1 + d2 + d3 + d4 - d5 - d6
f1 = - e1 * e2
f2 = e3**2
f3 = e4 / e3
rppr1 = f1 / f2 + f3
```

This is the Fortran code to calculate the Fréchet derivative of R_{PP} with respect to r_2.

```
ca = ( 1 + Q )
cb = ( r4 - Q )
cc = ( r4 - Q - 1 )
c1 = ( 1 + Q )**2
c2 = ( r4 - Q )**2
c3 = ( r4 - Q - 1 )**2
c4 = 8 * r2 * sin(theta)**2
d1 = - c4 * Q
d2 = r4 / r2 * T1 * T2**3
d3 = r4 / r2 * T1 * T224
d4 = cb * c4 * T1 * T3
d5 = cc * c4 * T0 * T1 * T2 * T3
d6 = c3 / r2 * T0 * T1 * T2**3 * T3
d7 = c3 / r2 * T0 * T1 * T2 * T3
d8 = - ca * c4 * T0 * T2
d9 = c1 / r2 * T0 * T2**3
d10 = c1 / r2 * T0 * T2
d11 = Q**2 + r4 * T1 * T2
d12 = c2 * T1 * T3
d13 = - r4 * T0 * T3
d14 = - c3 * T0 * T1 * T2 * T3
d15 = - c1 * T0 * T2
e1 = d1 + d2 + d3 + d4 + d5 + d6 + d7 + d8 + d9 + d10
e2 = d11 + d12 + d13 + d14 + d15
e3 = d11 + d12 - d13 - d14 - d15
e4 = d1 + d2 + d3 + d4 - d5 - d6 - d7 - d8 - d9 - d10
f1 = - e1 * e2
f2 = e3**2
f3 = e4 / e3
rppr2 = f1 / f2 + f3
```

This is the Fortran code to calculate the Fréchet derivative of R_{PP} with respect to r_3.

```
ca = ( 1 + Q )
cb = ( r4 - Q )
cc = ( r4 - Q - 1 )
c1 = ( 1 + Q )**2
c2 = ( r4 - Q )**2
c3 = ( r4 - Q - 1 )**2
c4 = 8 * r3 * r4 * sin(theta)**2
d1 = c4 * Q
d2 = - cb * c4 * T1 * T3
d3 = c2 / r3 * T1 * T3**3
d4 = c2 / r3 * T1 * T3
d5 = r4 / r3 * T0 * T3**3
d6 = r4 / r3 * T0 * T3
d7 = - cc * c4 * T0 * T1 * T2 * T3
d8 = c3 / r3 * T0 * T1 * T2 * T3**3
d9 = c3 / r3 * T0 * T1 * T2 * T325
d10 = ca * c4 * T0 * T2
d11 = Q**2 + r4 * T1 * T2
d12 = c2 * T1 * T3
d13 = - r4 * T0 * T3
d14 = - c3 * T0 * T1 * T2 * T3
d15 = - c1 * T0 * T2
e1 = d1 + d2 + d3 + d4 + d5 + d6 + d7 + d8 + d9 + d10
e2 = d11 + d12 + d13 + d14 + d15
e3 = d11 + d12 - d13 - d14 - d15
e4 = d1 + d2 + d3 + d4 - d5 - d6 - d7 - d8 - d9 - d10
f1 = - e1 * e2
f2 = e3**2
f3 = e4 / e3
rppr3 = f1 / f2 + f3
```

This is the Fortran code to calculate the Fréchet derivative of R_{PP} with respect to r_4.

```
ca = ( 1 + Q )
cb = ( r4 - Q )
cc = ( r4 - Q - 1 )
c1 = ( 1 + Q )**2
c2 = ( r4 - Q )**2
c3 = ( r4 - Q - 1 )**2
c4 = 4 * r3**2 * sin(theta)**2
c5 = 2 * ( 1 - 2 * r3**2 * sin(theta)**2 )
d1 = c4 * Q
d2 = T1 * T2
d3 = cb * c5 * T1 * T3
d4 = T0 * T3
d5 = cc * c5 * T0 * T1 * T2 * T3
d6 = ca * c4 * T0 * T2
d7 = Q**2 + r4 * T1 * T2
d8 = c2 * T1 * T3
d9 = - r4 * T0 * T3
d10 = - c3 * T0 * T1 * T2 * T3
d11 = - c1 * T0 * T2
e1 = d1 + d2 + d3 + d4 + d5 + d6
e2 = d7 + d8 + d9 + d10 + d11
e3 = d7 + d8 - d9 - d10 - d11
e4 = d1 + d2 + d3 - d4 - d5 - d6
f1 = - e1 * e2
f2 = e3**2
f3 = e4 / e3
rppr4 = f1 / f2 + f3
```